Applied Surface Science 601 (2022) 154171

Contents lists available at ScienceDirect

Applied Surface Science

journal homepage: www.elsevier.com/locate/apsusc

Full Length Article

The comparison of the corrosion behavior of the CrCoNi medium entropy alloy and CrMnFeCoNi high entropy alloy

Annica Wetzel [a], Marcus von der Au [a], Paul M. Dietrich [b], Jörg Radnik [a], Ozlem Ozcan [a], Julia Witt [a,*]

[a] Bundesanstalt für Materialforschung und -prüfung (BAM), D-12205 Berlin, Germany
[b] SPECS Surface Nano Analysis GmbH, D-13355 Berlin, Germany

ARTICLE INFO

Keywords:
Medium entropy alloy
High entropy alloy
SKPFM
XPS
Passivation
Corrosion

ABSTRACT

This work presents the determination of the corrosion characteristics of CrCoNi (medium entropy alloy) and CrMnFeCoNi (high entropy alloy) in 0.1 M NaCl and 0.1 M H_2SO_4. The morphology and chemical composition of the oxide layers formed on CrCoNi and CrMnFeCoNi were comparatively analyzed by scanning Kelvin probe microscopy (SKPFM) and scanning electron microscopy (SEM) and supported with chemical analysis by means of inductively coupled plasma mass spectrometry (ICP-MS) and X-Ray photoelectron spectroscopy (XPS). The analysis of the 3p core level peaks showed that the oxide layer (native and after anodic passivation) on CrCoNi consisted mainly of Cr oxides, while the oxide layer on CrMnFeCoNi was primarily composed of a mixture of Cr and Fe oxides. In addition, XPS was utilized to assess the oxide layer thicknesses. These results were compared to the thicknesses obtained by means of electrochemical impedance spectroscopy (EIS), with both approaches yielding values up to about 4 nm depending on the electrolyte and the alloy. Cyclic polarization measurements indicated superior corrosion resistance of CrCoNi in both aqueous environments compared to CrMnFeCoNi, as well as to AISI 304 stainless steel.

1. Introduction

In recent years high entropy alloys (HEAs) and especially medium entropy alloys (MEAs) have gained considerable attention in the material science community due to their outstanding properties such as good corrosion resistance [1,2] as well as a high wear resistance [3,4], thermal stability [5] and hardness [6]. HEAs and MEAs are multi-principal element alloys (MPEAs) that can be defined from either a compositional or a configurational perspective [7]. Based on the compositional definition, MEAs comprise 3 or 4 principal elements, while HEAs contain at least five principal elements, each in near equiatomic concentrations [8]. The high configurational entropy of this new type of alloys can lead to structural stabilization and the formation of a single-phase solid solution with no intermetallic phases that serve as nucleation sites for corrosion [6]. However, reports of HEAs forming complex microstructures and ordered intermetallic phases suggest that other factors such as atomic size differences and enthalpy of mixing also influence the stability of the solid solutions [9]. Another term, used interchangeably with HEAs due to the empirical nature of the definitions [10], is compositionally complex alloys (CCAs). This denotation allows a more general description that arises from the uncertainty on the role of configurational entropy [11]. Consequently, controversies exist, and these definitions serve as guidelines. In this work the terms HEA and MEA shall be used.

The use of MEAs and HEAs for industrial applications attracted wide attention. So far, extensive studies have focused on the alloy formation, crystallization processes, and mechanical and physical properties of multi principal element alloys. However, for the use as engineering materials, this new class of alloys must provide good corrosion resistance and electrochemical stability in industrial environments. Therefore, it is of great importance to investigate the corrosion behavior and susceptibility to safety–critical corrosion phenomena such as pitting corrosion of these alloys. While the corrosion and passivation behavior of CrMnFeCoNi has been studied in different media by many research groups, CrCoNi did not receive much attention so far, even though it has already been proven to have better properties than CrMnFeCoNi in terms of mechanical and thermal stability [12].

Previous studies on the corrosion behavior of HEAs have investigated

* Corresponding author.
E-mail address: julia.witt@bam.de (J. Witt).

https://doi.org/10.1016/j.apsusc.2022.154171
Received 12 April 2022; Received in revised form 1 July 2022; Accepted 2 July 2022
Available online 5 July 2022

the effects of different elements such as Al [13–16], Mn [17,18] and Cu [19,20]. Typical corrosion environments included aqueous solutions of H_2SO_4, NaCl and NaOH, whereas the HEA specimens generally demonstrated good corrosion resistance, with E_{corr}, E_{pit} and i_{corr} values similar to austenitic and ferritic stainless steels, as summarized by Birbillis et al. [1]. In their work Luo and Li et al. [21] compared the corrosion behavior and passive film properties of the HEA CrMnFeCoNi (Cantor alloy) with 304L stainless steel (304L SS) in 0.1 M H_2SO_4. Even though, the two alloys revealed a single-phase fcc crystal structure and similar corrosion resistant elements (i.e. Cr and Ni), the corrosion behavior of the two alloys differed. Due to the selective dissolution of Fe, a stable Cr-rich passive layer is known to form on the 304L SS surface. In case of the equimolar CrMnFeCoNi alloy, the authors found a comparable dissolution rate for all elements that favored the formation of a defective passive film with a lower corrosion resistance than that of 304L SS in 0.1 M H_2SO_4. Marcus and Mercier et al. [22] studied the composition and the thickness of the passive film on CrMnFeCoNi in the native state and after electrochemical exposure to 0.05 M H_2SO_4. They developed a new XPS approach based on the analysis of the 3p core level peaks. Combining this method with ToF-SIMS depth profiling experiments, it was possible to determine the presence of a duplex oxide structure consisting of Cr-, Fe- and Co-oxides in the outer layer and Cr- and Mn-oxides in the inner layer. The group also mentioned an increase in Cr-content after passivation and a decrease in the respective hydroxide species. In addition, the presence of a modified metallic layer enriched in Ni and Co was detected under the duplex oxide layer. Another study that employed XPS analysis to investigate the oxide film composition focused on the effect of Mn in the HEA when exposed to 0.1 M NaCl [17]. Herein, Torbati-Sarraf et al. found that the MEA CrFeCoNi forms a less-defective passive film with better anti-corrosion properties compared to the HEA CrMnFeCoNi. Most recently, Yang et al. [23] investigated the corrosion and passive film properties of the CrCoNi MEA which showed superior corrosion resistance in 1 M H_2SO_4 but inferior corrosion resistance in 1.5 M NaOH compared to AISI 304 stainless steel [23]. The main component of the oxide film in 1 M H_2SO_4 was Cr-oxide for CrCoNi and a mixture of Cr-oxide and Fe-hydroxide for AISI 304 stainless steel, indicating a selective dissolution. In 1.5 M NaOH CrCoNi exhibits intergranular corrosion and high dissolution of Cr, whereas AISI 304 forms a stabler and thicker film. Moreover, Bettini et al. [24] reported for CrCoMo alloy that the presence of Co resulted in a decrease in the onset of the oxygen evolution reaction (OER) leading to a lower breakdown potential.

In this work, the MEA CrCoNi and the HEA CrMnFeCoNi were investigated in 0.1 M NaCl and 0.1 M H_2SO_4 to clarify and compare their corrosion properties. The electrochemical behavior was monitored with cyclic potentiodynamic polarization (CPP) scans and revealed a superior corrosion resistance of the CrCoNi MEA compared to the CrMnFeCoNi HEA, as well as AISI 304 stainless steel (AISI 304), which was additionally used as a point of reference. For the first time, the XPS methodology based on the analysis of the 3p core level peaks was used to gain information on the chemical composition of the passive film and to determine the passive layer thicknesses of CrCoNi after anodic passivation. Thickness determination based on XPS and EIS confirmed the formation of a thicker oxide layer in NaCl than in H_2SO_4. Finally, atomic force microscopy (AFM) and scanning Kelvin probe force microscopy (SKPFM) served to study the morphology after corrosion which enabled the visualization of the corrosion mechanisms that occurred.

2. Material and methods

2.1. Sample preparation

The vacuum melted ingots of CrMnFeCoNi and CrCoNi were manufactured by the Laplanche group of Ruhr-University, Bochum, Germany. More detailed information on the alloy preparation and microstructural characteristics can be found elsewhere [25]. To briefly summarize, after casting, the CrMnFeCoNi and CrCoNi alloys were homogenized and recrystallized for 1 h at 1020 °C and 1060 °C, respectively. Both alloys exhibited a single-phase fcc microstructure with a 50 μm grain size on average [25]. Table 1 displays the chemical compositions of both alloys and was taken as reported in [26].

Austenitic stainless steel sheets (AISI 304, Goodfellow Cambridge Ltd., United Kingdom) were acquired as 1.2 mm thick sheets in the fully annealed condition and cut into coupons of 1.5 × 1.5 cm dimensions. In Table 2 the chemical compositions were summarized as reported in [27].

For further investigations alloy specimens were wet grounded consecutively with 600 to 4000 grit SiC paper (ATM GmbH, Germany) and subsequently polished with 3 μm and then 1 μm diamond pastes on respective polishing clothes (ATM GmbH, Germany). After the final polishing step, the samples were rinsed in an ultrasonic bath (Elmasonic P) in deionized water (0.055 μS cm^{-1}, Evoqua, USA) and then in acetone (ChemSolute, min. 99.5 %, Germany) for 5 min at 80 kHz to ensure the removal of any residues on the surface. Finally, the specimens were dried in an oil-free compressed air stream.

2.2. Electrochemical studies

Cyclic potentiodynamic polarization (CPP) measurements and electrochemical impedance spectroscopy (EIS) were performed at room temperature, using the Gamry Reference 600+ potentiostat (Gamry Instruments, C3 Prozess- und Analysentechnik GmbH, Germany) and the Gamry Framework data acquisition software (version 7.8.2). For the electrochemical testing a three-electrode set-up was utilized, with the alloy sample as the working electrode (WE), a coiled-up gold wire as the counter electrode (CE) and an Ag/AgCl electrode in 3 M NaCl as the reference electrode (RE). The potentials were referred to the used reference electrode. Prior to each measurement, the open circuit potential (OCP) was measured for 1800 s to reach equilibrium conditions. Electrochemical experiments were conducted in 10 ml of electrolyte solutions with a concentration of 0.1 M of either NaCl (ChemSolute, min. 99 %, p.a., Germany) or H_2SO_4 (AppliChem, 0.5 M, volumetric solution, Germany) prepared with deionized water.

To exclude interfering redox reactions, the cell was sealed, purged with N_2 for 30 min before and kept under an N_2-environment during testing. Before the electrochemical experiments were commenced, samples were cathodically conditioned at −1.00 V for 10 min. The CPP scan was run from an initial potential of −0.25 V vs. OCP to a final potential of 1.50 V vs. OCP for CrMnFeCoNi and CrCoNi and to 2.00 V vs. OCP for AISI 304 at a scan rate of 1 mV s^{-1}. If the current density reached a value of 5 mA cm^{-2} before the apex voltage, the scan was also reversed. Electrochemical passivation was achieved by applying a fixed potential for 3600 s in the passive polarization region identified by the CPP analysis (Table 3). EIS measurements were performed after OCP and after passivation experiments in the frequency range from 100000 Hz down to 0.1 Hz and with an applied AC voltage of 10 mV. The data analysis and equivalent electrical circuit (EEC) fitting for the electrochemical impedance spectra were conducted in Gamry EChem Analyst (version 7.8.2).

2.3. X-ray photoelectron spectroscopy (XPS):

XPS analyses were performed with a commercial spectrometer (SPECS Surface Nano Analysis GmbH, Germany) after electrochemical passivation. The spectra were acquired using a monochromatic Al Kα source ($h\nu = 1486.76$ eV) and a PHOIBOS 150 hemispherical analyzer combined with a 1D-CMOS detector. The angle between the X-ray source and the analyzer was 55° and the photoelectron emission angle was 0°. Charge compensation was done using a flood gun (FG22/35) emitting a beam of low energy electrons (3.5 eV, 75 μA) onto the sample. The analyzer was operated in fixed analyzer transmission (FAT) mode with a pass energy of 20 eV for the 3p core level and 50 eV for survey spectra.

Table 1
Chemical composition of CrCoNi (MEA) and CrMnFeCoNi (HEA) in atomic % determined by X-ray fluorescence analysis (XRFA) [25].

	Co	Cr	Fe	Mn	Ni	C	O	S
CrCoNi	33.30	32.53	0.95	0.09	32.85	0.019	0.226	0.004
CrMnFeCoNi	19.7	19.41	20.56	20.10	19.58	0.051	0.033	0.009

Table 2
Weight percentages wt% detected by inductively coupled plasma optical emission spectrometry [26].

	Mn	Cr	Ni	C	S, N, Si, P
AISI 304	0.97	18.52	8.02	0.035	≪1

Instrumental calibration and specification were done using a sputter cleaned Ag sample. The acquired spectra were fitted with CasaXPS (version 2.3.22PR1.0) using SPECS relative sensitivity factors (Supporting Information SI-2). The energy scales of the spectra were calibrated with the C1s peak to 284.8 eV. Furthermore, a Shirley-type background and a Gaussian-Lorentzian ratio GL(30) were employed for peak fitting.

2.4. Inductively coupled plasma mass spectrometry (ICP-MS):

ICP-MS measurements were performed to monitor and determine the dissolved metal concentrations after the CPP measurements. The analysis was conducted using the iCAP Q ICP-MS (Thermo Fischer Scientific, Germany) coupled to an ESI SC 4 DX Fast autosampler (Elemental Scientific, USA) and the Qtegra^{TM} software (Thermo Fischer Scientific, version 2.10.4345.64). The MS-system was tuned daily in accordance with the guidelines of te manufacturer. A 10 μg L^{-1} Rhodium solution (Merck, 1000 mg L^{-1} Certipur, Germany) was mixed on-line into the samples via the autosampler at a mixing ratio of approx. 1:10 to allow e. g., for drift corrections. A multi-element standard was used for external calibration (ICP-multi element standard IV (Certipur), Merck, Germany). For preparing the standards as well as the sample dilution, Type I reagent-grade water (18.2 MΩ cm) obtained from a Milli-Q-System (MerckMillipore, Germany) as well as HNO_3 (65 % p.A. (Chemsolute), Th Geyer, Germany (double sub-boiled)) were used prior to the analysis.

2.5. Scanning Kelvin probe force microscopy (SKPFM):

Freshly polished samples and samples after CPP experiments were studied by means of SKPFM under ambient conditions with a NanoWizard 4 (Bruker Nano GmbH, Germany - formerly known as JPK Instruments) operating with a resolution of 512x512 pixels. This technique was used to characterize the change of surface topography and potential after CPP measurements. For the first scan, the intermittent mode was used to collect the topography information, whereas during the second scan the tip was lifted by a predefined height of 30–40 nm and an AC voltage of 1.0 V was applied to the tip to determine the surface potential following the topography profile. The SKPFM images were collected at a scan frequency of 0.4–1.0 Hz using a silicon cantilever with a conductive Cr/Pt-coating (Tap300-G: nominal spring constant of 40 N m^{-1} (Budget Sensors, NanoAndMore GmbH, Germany). The software JPK Data Processing Suite (version 6.1.88) was used for offline analysis of the surface topography and the potential. Image flattening was performed with the first order least-square polynomial function, which removes tilt and the vertical z-offset between line scans. As no absolute reference was used in SKPFM analysis, the reported values are potential differences.

3. Results and discussion

3.1. Electrochemical corrosion behavior

The cyclic potentiodynamic polarization (CPP) method and electrochemical impedance spectroscopy (EIS) were used to characterize the corrosion performance of the CrCoNi MEA and the CrMnFeCoNi HEA. The results were compared to the corrosion behavior of AISI 304, which was additionally used as a point of reference. The CPP plots recorded 0.1 M H_2SO_4 and 0.1 M NaCl are presented in Fig. 1. The determined breakdown potential E_b, corrosion potential $E_{corr,}$ and passive region ΔE values are summarized in Table 3 along with the respective values for i_{corr}. The E_{corr} and i_{corr} values (Table 3) were obtained by extrapolation of the linear segments of the cathodic Tafel slope [28]. CrCoNi exhibited the highest E_{corr} in both NaCl and H_2SO_4 and the lowest i_{corr} in NaCl, indicating a better corrosion resistance in comparison to the HEA. In H_2SO_4, CrCoNi and CrMnFeCoNi displayed nearly identical i_{corr} values. AISI 304 showed the lowest E_{corr} and highest i_{corr} values in both electrolytes. It should be noted, that E_{corr} values of all three alloys were nobler in NaCl relative to H_2SO_4, and higher values were observed for i_{corr}.

The CPP data for CrCoNi in 0.1 M H_2SO_4 (Fig. 1a) revealed the lowest current densities in the passive region suggesting that the oxide layer formed is more stable than that on CrMnFeCoNi and AISI 304. The extent of the passive region in the forward scan were similar for all three alloys. The sharp increase in the anodic current indicated the breakdown of the passivity and the dissolution of the previously formed protective oxide layer. During the degradation of the oxide layer other redox reactions, especially the oxygen evolution reaction (OER, $E^0 = 1.23$ V), can contribute to the total current density [24,29]. As a result, the formation of higher valence oxide species and the development of localized corrosion sites may occur [29,30]. A study by Bettini et al. [24] found that for the high corrosion resistant CoCrMo alloys only approximately 40 % of the total current density observed at high anodic potentials arose due to metal dissolution, and that the OER also contributed to the total transferred charge. They further argued that Co is a known catalyst for the electrochemical water oxidation [24] which may decrease the overpotential of the OER [24], potentially leading to the observed lower breakdown potentials ($E_b < 1.23$ V vs. SHE) [31]. The absence of a hysteresis loop on the reversed scan for CrCoNi and CrMnFeCoNi in this study suggests that no localized corrosion occurred and indicate an active surface and general corrosion (Fig. 1a). AISI 304, on the other

Table 3
Corrosion parameters obtained from the CPP plots (Fig. 1) for the respective alloys and electrolytes.

	E_{corr} [V]		ΔE [V]		E_{pass} [V]		i_{corr} [A cm^{-2}]	
	H_2SO_4	NaCl	H_2SO_4	NaCl	H_2SO_4	NaCl	H_2SO_4	NaCl
CrCoNi	−0.30	−0.11	≈−0.21–0.83	≈0.05–0.60	0.40	0.32	3.43×10^{-6}	3.63×10^{-8}
CrMnFeCoNi	−0.38	−0.19	≈−0.20–0.77	≈−0.05–0.06	0.25	0.01	3.35×10^{-6}	8.75×10^{-8}
AISI 304	−0.40	−0.27	≈−0.27–0.75	≈−0.15–0.40	0.35	0.15	7.37×10^{-6}	2.44×10^{-7}

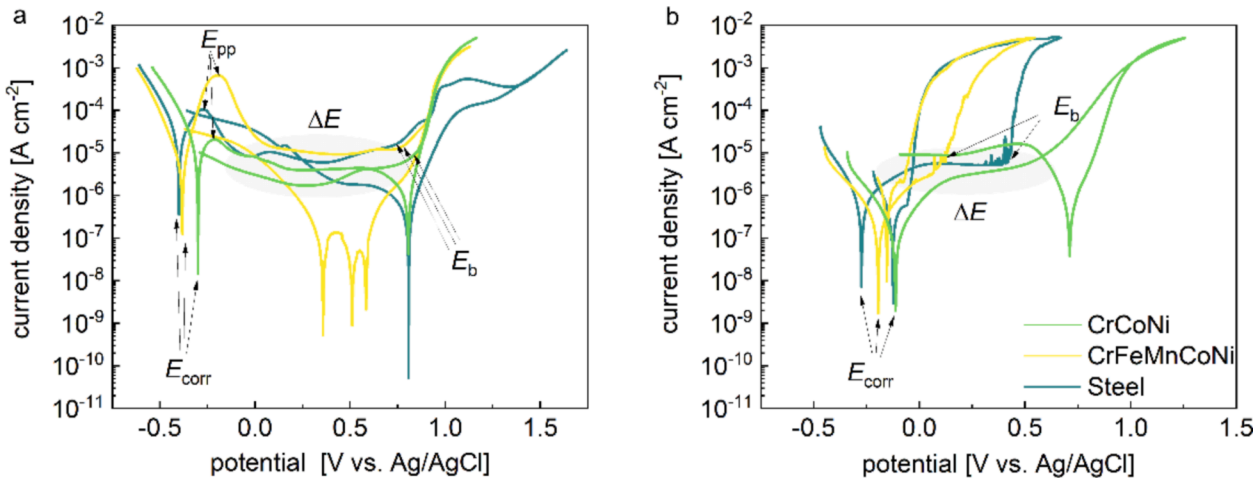

Fig. 1. CPP plots for CrCoNi, CrMnFeCoNi and AISI304 in a) 0.1 M H_2SO_4 and b) 0.1 M NaCl. The corrosion parameters E_{corr} and ΔE indicated in the diagrams are summarized in Table 3.

hand, produced a pronounced negative hysteresis, indicating that the anodic reactions at the surface slowed down on the reversed scan, possibly due to the formation a passive film in agreement with the literature [24]. The reversed scan of CrCoNi in H_2SO_4 was close to the forward scan after the anodic/cathodic transition which demonstrates that a similar degree of passivation prevailed within the passive region [32]. Only one anodic/cathodic transition was observed for CrCoNi and AISI 304 on the reverse scan, which occurred at the same potential. CrMnFeCoNi demonstrated several transition peaks on the reverse scan which may be a sign of electrochemical activity at or within the oxide film. The reversed scan also displayed lower values in current density, suggesting a stronger passivation than on the forward scan. This behavior could be due to the higher available concentrations of O_2, which accumulated close to the electrode surface during polarization at very high anodic potentials [33]. Further research is currently ongoing to investigate the decrease in current density during the reverse scan and the role of O_2.

The CPP data (Fig. 1b) for CrCoNi in 0.1 M NaCl showed the broadest passive region, demonstrating the formation of a stable passive film. Compared to its behavior in H_2SO_4, no pre-passivation peak was observed which indicated a spontaneous passivation [32,34]. Furthermore, a negative hysteresis was observed, with a crossover of the forward and reversed scan occuring at ~ 0.60 V. In contrast, CrMnFeCoNi and AISI 304 were more susceptible to localized corrosion in 0.1 M NaCl than CrCoNi. Both displayed a positive hysteresis on the reversed scan, suggesting pitting corrosion [32]. However, the passive region for CrMnFeCoNi was much smaller than for AISI 304 with a breakdown potential about 0.36 V lower. This could indicate a lower pitting corrosion resistance in CrMnFeCoNi. In addition, the passive region showed an irregularly fluctuating current response caused by local breakdown and repassivation within the oxide layer, which was also observed in AISI 304, but at higher potentials. This behavior indicates a metastable passive layer and was detected by Yang and Liaw et al. [34] for Al_xCoCrFeNi HEAs in 3.5 wt% NaCl. In comparison to CrMnFeCoNi, the onset of anodic corrosion for AISI 304 is clearly visible due to the strong increase of the current density at the breakdown potential of 0.42 V, indicating a faster breakdown of the protective oxide film, which was further confirmed by the large area enclosed within its positive hysteresis loop [35]. In contrast, for CrCoNi, the current steadily increased above 0.50 V with no discernable breakdown potential observed, confirming its superior corrosion resistance in NaCl.

Electrochemical impedance (Z) is the complex combination of various processes that are either of a resistive, capacitive and/or inductive nature. These processes can be modeled through electrical equivalent circuits (EEC) using an electrical circuit analogy [36]. In this study, the empirical EEC in Fig. 2 was employed to fit and analyze the experimental impedance data after either keeping the sample at OCP, or after anodic passivation. The EEC was first used by Joiret et al. [37], whereas the application by Orazem et al. [38] for the surface analysis of ASTM A416 steel exchanged the capacitance element with a constant phase element, which was also employed in this work. More recently, the EEC was also employed in other high entropy studies [39,40]. To ensure a good fitting quality, chi square values were below 10^{-3} orders of magnitude [21]. The EEC model (Fig. 2) comprises of a resistor R_s for the resistance of the electrolyte and is connected in series with a parallel combination of constant phase element CPE_{dl} and resistor R_{ct}, whereas the latter accounts for the faradaic reaction occurring at the interface of the dielectric layer and electrolyte. Another parallel combination of constant phase element CPE_f and resistor R_f follows, considering the heterogenous and potentially porous nature of the dielectric passive layer [38]. It was assumed that the resistivity of the passive film is normal to the electrode surface. Fig. 3 displays the respective Bode plots and the fitted data are summarized in Tab. SI-1. For all three alloys, R_s can be observed at high frequencies (Fig. 3) with a phase angle approaching 0°. The phase angles of all three alloys reached their minimum at medium frequencies and in general, remained above −90°. Furthermore, the gradients of their impedance moduli (grad|Z|), at medium frequencies, stayed below unity, which confirms the pseudo-capacitive nature of the examined electrochemical systems [41]. The modulus of impedance at 0.1 Hz ($|Z|_{0.1Hz}$) typically correlated to the polarization resistance R_p of the alloy indicating its corrosion resistance [42]. R_p can be derived from the fitted EIS data, where $R_p = R_s + R_{ct} + R_f$ [23]. The observed $|Z|_{0.1Hz}$ and calculated R_p values correspond for all examined electrochemical systems (Table SI-1).

In H_2SO_4, $|Z|_{0.1Hz}$ increased for the alloys from OCP to passivation

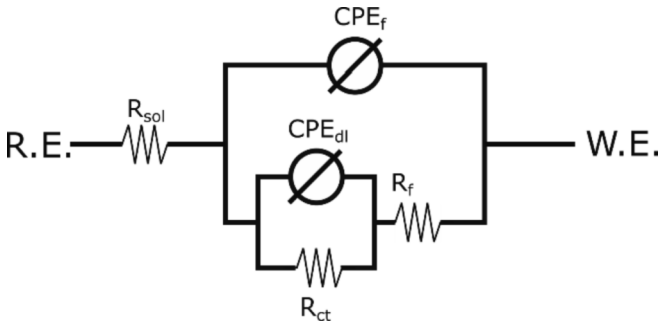

Fig. 2. Empirical EEC model employed to fit the experimental impedance data.

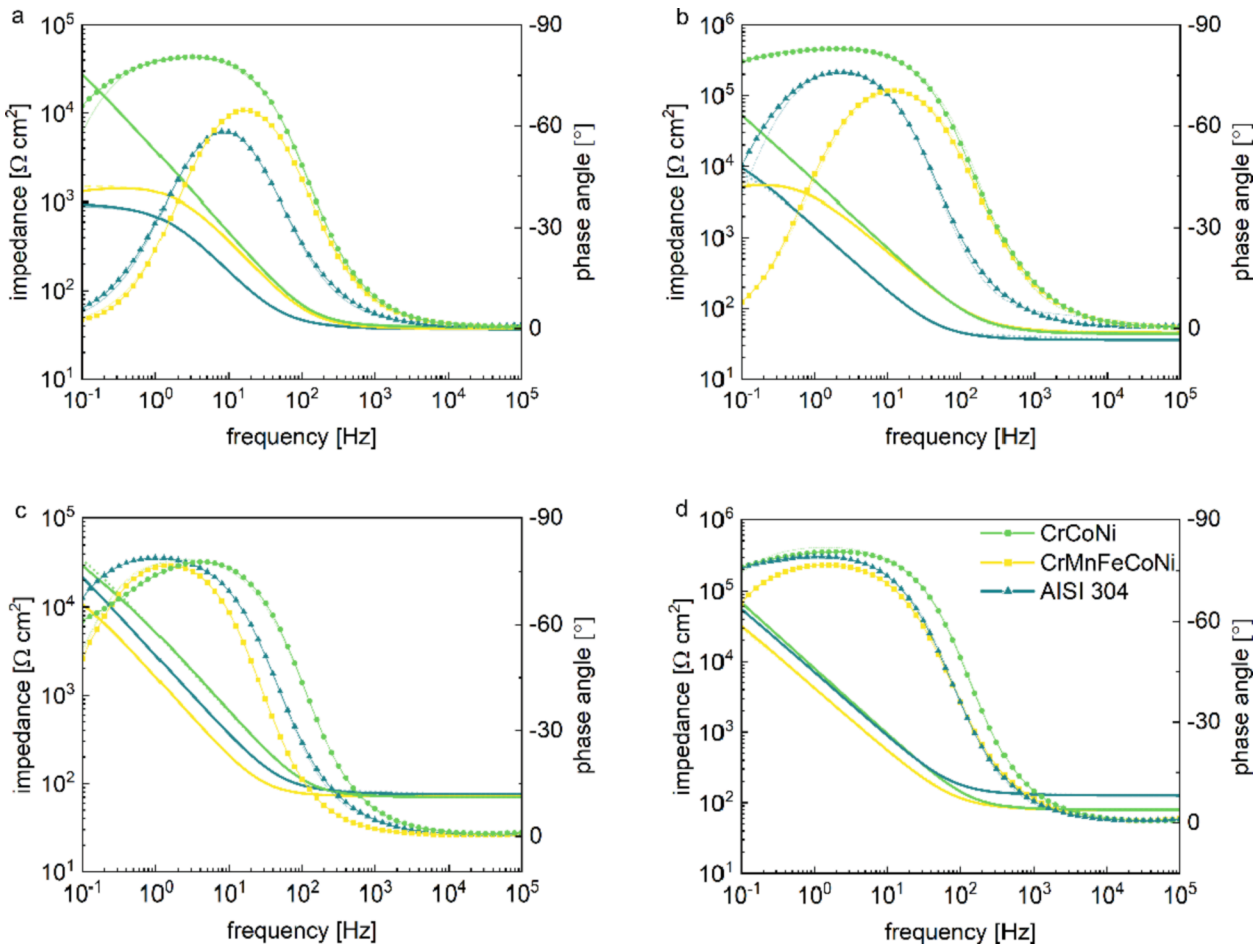

Fig. 3. EIS Bode plots recorded for CrCoNi, CrMnFeCoNi and AIS 304 in 0.1 M H_2SO_4 after (a) OCP and (b) anodic passivation and in 0.1 M NaCl after (c) OCP and d) anodic passivation. The fits with the EEC of Fig. 2 are presented by dotted lines.

(Fig. 3a and b). In the EIS spectra after the OCP, the phase angles at low frequencies approached 0° and reached minimum values below −70° with small broadening at medium frequencies (Fig. 3a). This result demonstrated that no stable passive film has formed for any of the alloys after OCP treatment. After passivation, however, the data suggested that stabler passive films have formed. The minimum phase angles reached levels ≤ −70° (Fig. 3b), disclosing a more capacitor-like nature. The most stable film was observed for CrCoNi with the most predominant broadening in the phase angle signal at medium frequencies, as well as the highest $|Z|_{0.1Hz}$. These observations correlated with the R_{ct} and R_p values obtained from fitting the impedance data (Tab. SI-1) to EEC in Fig. 2, where CrCoNi displayed the most substantial increase compared to the other two alloys, confirming a superior corrosion resistance.

In NaCl, similar trends were observed for all three alloys, with $|Z|_{0.1Hz}$ values increasing and and phase angle traces broadening after passivation (Fig. 3c and d). Even though the increase in polarization resistance ($|Z|_{0.1Hz}$) was not as distinct as in H_2SO_4, higher values of $|Z|_{0.1Hz}$ were reached in NaCl for all three alloys after the OCP and the anodic passivation (Fig. 3). The minimum phase angles in NaCl were close to −80° after OCP and passivation, suggesting a more capacitor-like behavior in the Cl^--ion containing electrolyte and confirming the instantaneous passivation of the alloys, as was determined in the CPP scans (Fig. 1). After OCP, the phase angles did not show the same approach to 0° at low frequencies as was found for H_2SO_4, which corroborated passivation at corrosion potential for all three systems (Fig. 3c). The broadening of the phase angle signal after passivation indicated the growth of a passive film (Fig. 3d). However, the phase angles decreased only marginally for CrCoNi and AISI 304 after passivation and increased slightly for CrMnFeCoNi. The data for CrMnFeCoNi and AISI 304 suggested that the surfaces of these alloys were already passivated during the OCP measurements and were further passivated after anodic passivation. This was in correlation with the CPP responses (Fig. 1) that indicated metastable pitting within the passive range for both alloy systems. CrCoNi, on the other hand, showed a significant increase in its passive film stability. Again, this observation correlated to the R_{ct} and R_p values, which can be found in the Supporting Information (Tab. SI-1), where CrCoNi demonstrated the most predominant increases after active passivation.

Furthermore, EIS data were used to determine the passive film thickness. According to Eq. (1) [43], the thicknesses were obtained by

$$C_f = \frac{\varepsilon\varepsilon_0}{\delta_{oxide}} \quad (1)$$

where C_f is the capacitance of the oxide film measured at frequency f_{max}, ε_0 is the vacuum permittivity (8.854×10^{-14} F cm^{-1}), ε is the relative permittivity of the passive film and assumed to be 30 based on [40,44,45] and δ_{oxide} is the oxide film thickness.

The respective capacitances were determined from the CPE_f data listed in the Supporting Information (Tab. SI-1) using Eq. (2) [43], where f_{max} is the frequency at the largest phase angle [27].

$$C_f = CPE_f(2\pi f_{max})^{m-1} g; \text{where} g = 1 + 2.88(1-m)^{2.375} \quad (2)$$

In general, films after passivation were about 1 nm thicker than those after the OCP measurements (Table 4). CrCoNi revealed the thickest film after passivation in NaCl with 3.2 nm and a slightly thinner film with 3.1 nm after passivation in H_2SO_4. The CrMnFeCoNi HEA, on the other

Table 4
Summary of the derived film capacitance and the respective oxide layer thickness.

		C_f [F cm^{-2}]	δ_{oxide} [nm]
OCP			
H_2SO_4	CrCoNi	1.30×10^{-5}	2.1
	CrMnFeCoNi	1.21×10^{-5}	2.2
NaCl	CrCoNi	1.23x x10^{-5}	2.2
	CrMnFeCoNi	1.28×10^{-5}	2.1
Anodic passivation			
H_2SO_4	CrCoNi	8.69×10^{-6}	3.1
	CrMnFeCoNi	8.45×10^{-6}	3.1
NaCl	CrCoNi	8.20×10^{-6}	3.2
	CrMnFeCoNi	9.12×10^{-6}	2.9

hand, formed its thickest film after passivation in H_2SO_4 with 3.1 nm. In NaCl its oxide layer showed the lowest of all measured thicknesses with 2.9 nm which correlates with the electrochemical findings discussed above.

3.2. Chemical composition of the passive films

XPS and ICP-MS analyses were conducted to obtain information on the composition of the oxide film on the alloys and dissolved species during CPP experiments, respectively. XPS analyses have already been reported in the literature on HEA and MEA systems [21–23,46] and have proven efficient in studying oxide layers in the nanometer range [22,47–49]. However, as discussed by Marcus and Mercier et al. [22], the strong interference of various Auger transitions with the 2p core level peaks of the transition metals, renders their analysis a very challenging task. Within the present study, the 3p core level peaks with binding energies ranging between 38.0 eV and 72.0 eV were used to quantify the individual components of the oxide layer on the native and electrochemically treated alloy surfaces and to calculate the oxide layer thicknesses.

Fig. 4 shows the 3p core level spectra recorded on the surface CrCoNi, CrMnFeCoNi and AISI 304 after anodic passivation with the detected elements and their relative proportions in atomic percentage. The resulting fitting parameters of the XPS spectra are listed in the Supporting Information in Tab. SI-3. The recorded spectra and fitted peak positions agreed with the data reported by Marcus and Mercier et al. [22]. The Cr 3p core level peaks were fitted with two components corresponding to Cr_{ox} (BE = 43.5 eV) and Cr_{met} (BE = 41.3 eV). The Fe 3p peaks showed three components, representing the metal species Fe_{met} (BE = 52.1 eV) and its oxides Fe^{3+} (BE = 55.3 eV) and Fe^{2+} (BE = 53.3 eV) [50]. Our results differ slightly from the results of Marcus and Mercier, as they discussed only one oxide species in their work. In the light of very recent work, the possibility of a differentiation of Fe^{3+} and Fe^{2+} in the Fe 3p spectra is controversial [51]. In our analysis, a satisfactory peak fitting was not possible without the consideration of both oxidation states. Due to the compositional complexity of the studied materials, a systematic analysis of the Fe oxides species was not possible. Thus, the authors opted for considering the Fe oxide contribution with a differentiation of the oxide species in the discussion. Further studies are needed to analyze the distribution of Fe^{3+} and Fe^{2+} in the oxide film. The Co 3p and Mn 3p peaks were composed of a metallic (BE = 58.5 eV and 46.5 eV) and an oxide (BE = 59.8 eV and 48.0 eV) component. Ni displayed a clear spin orbit coupling effect with separated Ni $3p_{3/2}$ (BE = 66.0 eV) and Ni $3p_{1/2}$ (BE = 68.0 eV) contributions and thus, it can be assumed that the Ni 3p components are fully metallic (BE = 66.0 eV) [22]. Also, previous studies on stainless steels and CrMnFeCoNi have shown that Ni enriches in its metallic form beneath the surface oxide layer [22,49,52].

For all studied alloys, it is evident that after passivation the oxides predominated the metallic components at the topmost layer. For CrCoNi and CrMnFeCoNi, the ratio of oxide to metallic components was largest after H_2SO_4, approaching to 2:1 and 1.3:1, respectively. All alloys showed an increase in Cr oxides after passivation. Ni was the prevalent constituent within the metallic components, suggesting that the oxide layer formed is relatively thin. Especially for CrCoNi, Ni represented half of the metallic components after passivation. According to Marcus and Mercier et al. [22], oxide layer thicknesses range between 1.4 and 2 nm for CrMnFeCoNi after electrochemical treatment in 0.05 M H_2SO_4. The amount of Fe oxides species in the passive film on CrMnFeCoNi increased in H_2SO_4 and decreased in NaCl. Furthermore, only two component peaks Fe_{met} and Fe^{2+} were observed in the XPS spectrum after anodic passivation in NaCl, indicating that different corrosion behaviors exist in the different electrolytes. XPS analyses further revealed the presence of sulfur on the alloy surfaces when treated with H_2SO_4, which may imply the adsorption of SO_4^{2-} (Fig. SI-4 in Supporting Information).

To determine the passive film thicknesses, a homogeneous and continuous oxide layer was assumed. The thicknesses were calculated according to [22] with Eqs. (3-5).

$$I_X^{met} = k\sigma_X\lambda_X^{Met}D_X^{Met}T_X\exp(-\frac{\delta_{oxide}}{\lambda_X^{Ox}} \quad (3)$$

$$I_Z^{Ox} = k\sigma_Z\lambda_Z^{Ox}D_Z^{Ox}T_Z[1-\exp(-\frac{\delta_{oxide}}{\lambda_Z^{Ox}} \quad (4)$$

$$\delta_{oxide} = ln\left(\frac{I_Z^{Ox}\lambda_X^{met}D_X^{met}}{I_{ox}^{met}\lambda_Z^{Ox}D_Z^{Ox}}+1\right)*\lambda_X^{Ox} \quad (5)$$

where I_Z^Y is the intensity of photoelectrons emitted by the core level Z in matrix Y, k is a specific spectrometer constant, σ is the photoionization cross-section (SI-2), λ_Z^Y is the inelastic mean free path (IMFP), T_X is the transmission function of the PHOIBOS analyzer, which is considered to be constant over the energy range used for the conducted measurements herein, D_Z^Y is the density of element Z in matrix Y given by $D_Z^Y = \frac{\rho_Y}{M_Y}x_Z^Y$ where ρ_Y is the density of matrix Y, M_Y is the molecular weight of matrix Y and x_Z^Y is the atomic percentage of element Z in matrix Y and δ_{oxide} is the oxide layer thickness [22]. The assumed oxide densities and IMFPs are summarized in SI-5. IMFPs were calculated via the TTP-2 formula [53] and double checked with the NIST database [54].

Table 5 displays the resulting passive layer thicknesses. The thickness of the native oxide film of CrCoNi (2.5 nm) was slightly thinner than that of CrMnFeCoNi (2.8 nm). After anodic passivation, the oxide film thicknesses generally increased by approximately 1 nm for both alloys. CrCoNi possessed a thicker oxide layer with 3.9 nm in NaCl than in H_2SO_4 (3.2 nm), while CrMnFeCoNi was found to have the same thickness in both electrolytes of 3.7 nm. The resulting δ_{oxide} agreed with the previously determined film thicknesses using EIS (Table 4) and the increase in δ_{oxide} confirmed the formation of thicker protective oxide films after anodic passivation. The differences between the δ_{oxide} values determined by impedance and XPS measurements were approximately 0.6 nm, which corresponds to about 20 % difference. This result agrees with the previously discussed estimated relative uncertainties of about 15 % for the IMFPs [53] and about 10 % for the relative sensitivity factors [55].

The collected ICP-MS data provided a further understanding of the corrosion processes occurring at the CrCoFeMnNi and CrCoNi surface during the CPP measurements and complement the XPS analyses. Table 6 shows the distribution of metal concentration in µM for the respective alloys. The bar graph representation in Fig. 5 shows the percentages of dissolved metal ions in NaCl and H_2SO_4 of all three alloys. For all alloy systems the concentration of dissolved metal ions was found to be higher in NaCl than in H_2SO_4 solution (Tabe 6) indicating a more severe corrosion attack in the Cl^--ion containing electrolyte. The relative dissolution of Cr ions, compared to the other metals, was slightly higher in 0.1 M H_2SO_4 for CrCoNi and CrMnFeCoNi. This result

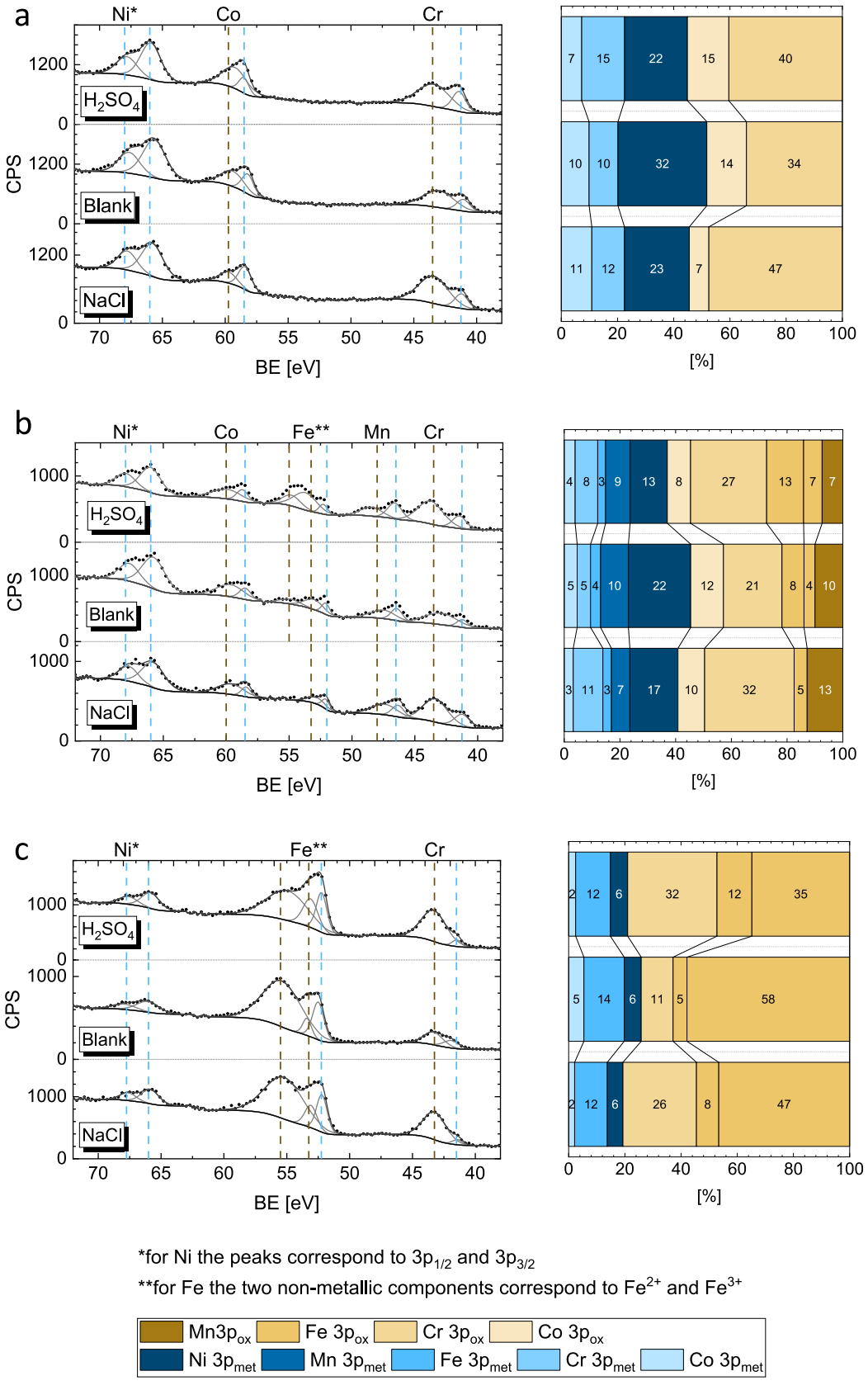

Fig. 4. 3p XPS spectra of (a) CrCoNi, (b) CrMnFeCoNi and (c) AISI 304 are displayed with the respective component fits (left) and the distribution in atomic-% of each component after the corresponding electrolyte treatment (right).

Table 5
Summary of the oxide layer thicknesses derived from the XPS results for CrCoNi and CrMnFeCoNi in the native state and after anodic passivation in 0.1 M H_2SO_4 and 0.1 M NaCl.

		δ_{oxide}[nm]
Native state		
	CrCoNi	2.5
	CrMnFeCoNi	2.8
Anodic passivation		
H_2SO_4	CrCoNi	3.2
	CrMnFeCoNi	3.7
NaCl	CrCoNi	3.9
	CrMnFeCoNi	3.7

Table 6
Summary of the elemental dissolution concentrations after CPP in a 0.1 M NaCl and 0.1 M H_2SO_4.

		Cr [μM]	Co [μM]	Ni [μM]	Fe [μM]	Mn [μM]
NaCl	CrCoNi	94.71	101.5	101.51	–	–
	CrMnFeCoNi	65.82	84.23	79.87	40.72	93.47
	AISI 304	78.31	–	48.99	346.87	9.39
H_2SO_4	CrCoNi	76.42	72.44	75.42	–	–
	CrMnFeCoNi	34.93	36.72	37.53	15.38	36.46
	AISI 304	31.59	–	12.94	95.30	2.06

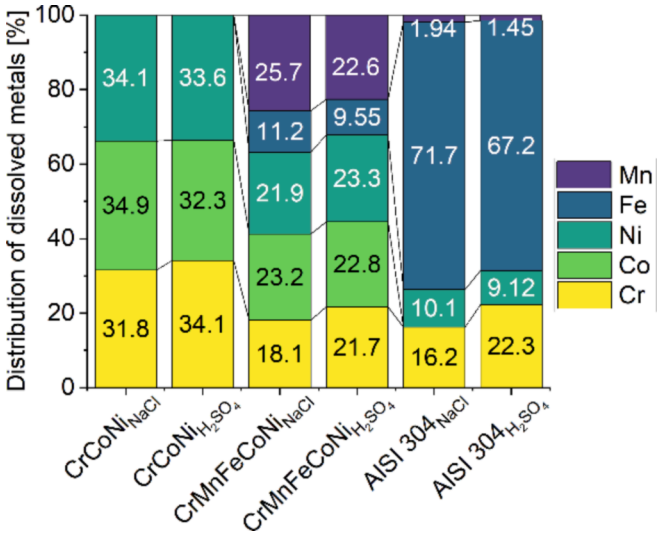

Fig. 5. The percentages of the concentration distribution of the individual metals in solution after CPP measurements.

correlated to the oxide compositions found by XPS, where a higher relative concentration of Cr oxide was found on the sample surfaces after the electrochemical treatment in NaCl. For CrMnFeCoNi, however, more Fe dissolved in NaCl compared to H_2SO_4, which is also reflected by the lower Fe oxide species on the surface. It should be noted that the concentrations of Cr, Mn, Co and Ni were near the stoichiometric chemical compositions in solution as in the bulk HEA. In comparison to the HEA and AISI 304, the XPS results for MEA CrCoNi revealed the highest metal to oxide ratios, indicating the formation of an oxide layer that may be thinner than that for CrMnFeCoNi which was the case after passivation in H_2SO_4 (Table 5). In the NaCl and H_2SO_4 solution, CrCoNi showed similar dissolution concentrations for all three metals (Table 6) that were also proportional to their stoichiometry within the alloy. No metal in the MEA dissolved preferentially. Bettini et al. [24] argued for CrCoMo alloys that the nearly equal concentration between the alloy and the dissolved metal species is related to dissolution at microstructural weak points and not to the uniform dissolution of the protective oxide layer. These findings and the results presented here may provide further evidence that the observed increase in total anodic current after The breakdown potential, as can be seen in Fig. 1, was also driven by other processes, such as the OER. Higher Cr (and Fe for CrMnFeCoNi) concentrations are generally associated with dissolution or breakdown of the passive layer [24], which were not observed within this study.

3.3. Morphology of the polarized surfaces

SKPFM studies were performed ex-situ to understand the corrosion mechanisms and to characterize the changes to the surface topography and potential of CrCoNi and CrMnFeCoNi in corrosive environments. Fig. 6 shows the SKPFM images of CrCoNi and CrMnFeCoNi before and after CCP measurements in 0.1 M H_2SO_4 and 0.1 M NaCl.

The topography of the bare CrCoNi and CrMnFeCoNi surfaces was dominated by polishing scratches with a maximum depth of<10 nm (Fig. 6a, b). Moreover, inclusions, containing Cr oxide, protruded from the polished surfaces and showed a higher (nobler) potential relative to the alloy matrix due to the presence of an oxide layer on top of the inclusions. The topography image in Fig. 6d demonstrate that CrMnFeCoNi was susceptible to general corrosion in a 0.1 M H_2SO_4 electrolyte solution as the alloy uniformly dissolved over the entire surface. The larger cavities may be a result of localized dissolution or mechanical abrasion through polishing of the Cr oxide inclusion. In addition, SEM studies showed accelerated anodic corrosion around the Cr-oxide inclusion, which could be explained with Cr depletion around the particle during the formation of the inclusion (Fig. SI-6c in Supporting Information). The Volta potential map identified a higher potential on the alloy matrix around the remaining cavity, which could be caused by the formation of an oxide film during the corrosion process. A different corrosion mechanism was observed for CrMnFeCoNi in an electrolyte solution containing Cl^--anions. Fig. 6f presents the topography of CrMnFeCoNi after polarization in a 0.1 M NaCl electrolyte solution, revealing the initialization of a localized corrosion attack which lead to the formation of deeper pits in the micrometer range. These pits could not be investigated with the atomic force microscope due to their larger size, however, they could be clearly identified by SEM (Fig. SI-6d in Supporting Information). There is correlation between this result and the electrochemical studies, where a typical pitting hysteresis was observed during the polarization of CrMnFeCoNi in NaCl (Fig. 1b, yellow line). In contrast to CrMnFeCoNi, CrCoNi showed a uniform corrosive attack over the entire surface area in both electrolytes (Fig. 6c, e). Moreover, intergranular corrosion of immediately adjacent grain boundaries was observed for CrCoNi, and this attack is more pronounced in the NaCl electrolyte solution than in H_2SO_4. These findings were confirmed by SEM images shown in the Supporting Information in Fig. SI-6a, b. Furthermore, the Volta potential maps identify a higher potential at the grain boundaries which might be caused by the formation of an oxide layer during the corrosion process.

4. Conclusion

The corrosion behavior and composition of the passive films of the CoCrNi MEA and the CrMnFeCoNi HEA in 0.1 M H_2SO_4 and 0.1 M NaCl were studied in detail by electrochemical techniques combined with XPS and AFM analysis. The following conclusions can be made:

1. Electrochemical analysis clearly indicates a superior corrosion behavior of CrCoNi MEA in both electrolytes in comparison to the CrFeMnCoNi HEA, as well as AISI 304 stainless steel. SKPFM and SEM studies confirmed the high susceptibility of CrMnFeCoNi to pitting corrosion in NaCl, with general corrosion observed in H_2SO_4. CrCoNi experienced general and intergranular corrosion in both

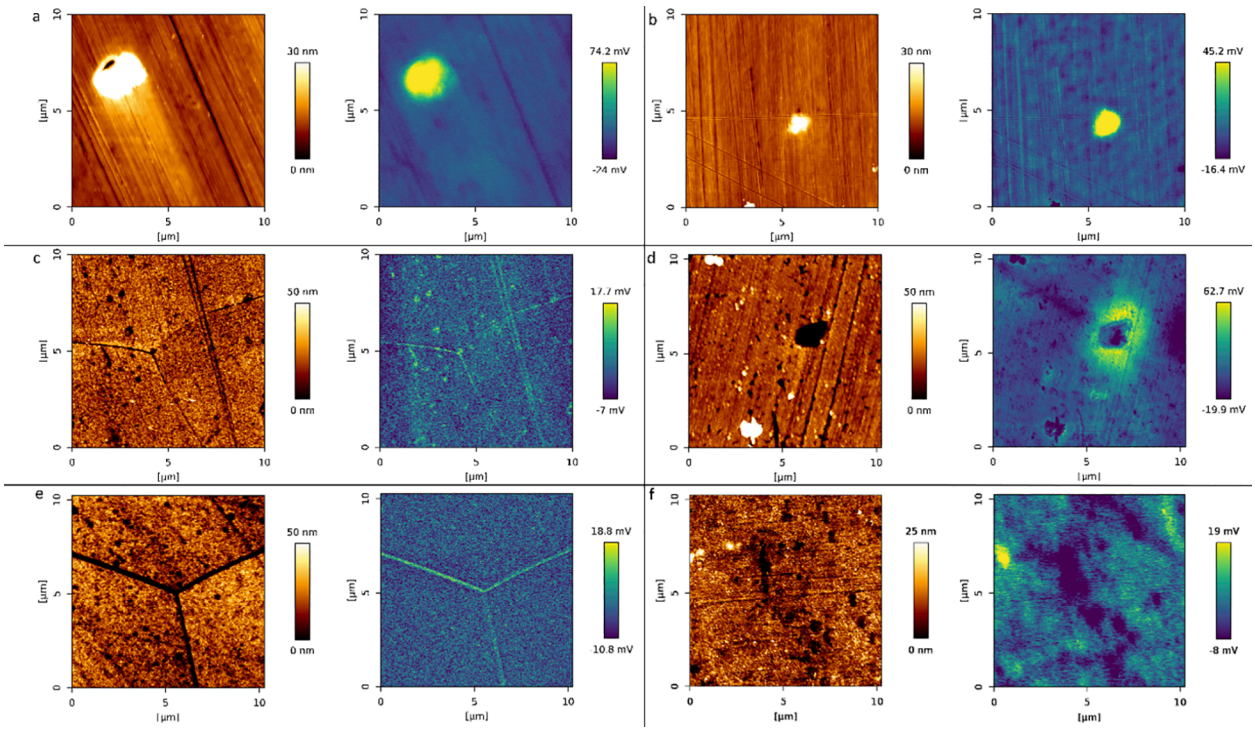

Fig. 6. SKPFM images demonstrate the topography (left) and potential (right) of a (a) CroCNi and (b) CrMnFeCoNi surface before and after CCP measurements in 0.1 M H_2SO_4 (c) CrCoNi and (d) CrMnFeCoNi and 0.1 M NaCl (e) CrCoNi and (f) CrMnFeCoNi.

electrolyte solutions. Considering the high corrosion resistance and low onset potential for OER, CrCoNi has a great potential to be used as an OER anode material. Ongoing studies focus on the long-term stability of both alloys.

2. XPS 3p core level peak analysis revealed that the oxide layer (native and after anodic passivation) formed on CrCoNi consists mainly of Cr oxides. The oxide layer on CrMnFeCoNi, on the other hand, is primarily composed of Cr and Fe oxides. Furthermore, a higher relative concentration of Cr oxide was found on the sample surfaces of both alloys after the electrochemical treatment in NaCl. ICP-MS measurements confirmed the higher release of Cr ions in 0.1 M H_2SO_4.
3. The calculated oxide layer thicknesses using XPS and EIS showed comparable values up to about 4 nm depending on electrolyte and alloy. CrCoNi possessed a thicker oxide layer in NaCl than in H_2SO_4, with Cantor reaching similar values for film thicknesses in both electrolytes.

The author PMD was employed by the company SPECS Surface Nano Analysis GmbH.

The remaining authors declare that they have no known competing financial interests or personal relationships that could have appeared to influence the work reported in this paper.

CRediT authorship contribution statement

Annica Wetzel: Investigation, Validation, Methodology, Visualization, Writing – original draft. **Marcus von der Au:** Investigation. **Paul M. Dietrich:** Investigation. **Jörg Radnik:** Investigation. **Ozlem Ozcan:** Supervision, Resources. **Julia Witt:** Conceptualization, Methodology, Visualization, Writing – original draft, Supervision.

Declaration of Competing Interest

The authors declare that they have no known competing financial interests or personal relationships that could have appeared to influence the work reported in this paper.

Acknowledgements

The authors want to thank Prof. Guillaume Laplanche and co-workers from Ruhr-University, Bochum, Germany for providing the alloy materials. The authors greatly acknowledge funding from the Bundesanstalt für Materialforschung und -prüfung (BAM), Berlin, Germany through the PhD Program.

Data Availability

The raw/processed data required to reproduce these findings will be made available on request.

Funding source

This research did not receive any specific grant from funding agencies in the public, commercial, or not-for-profit sectors.

Appendix A. Supplementary material

Supplementary data to this article can be found online at https://doi.org/10.1016/j.apsusc.2022.154171.

References

[1] Y. Qiu, S. Thomas, M.A. Gibson, H.L. Fraser, N. Birbilis, Corrosion of high entropy alloys, Npj Mat. Degrad 1 (2017) 15, https://doi.org/10.1038/s41529-017-0009-y.
[2] Y.Z. Shi, B. Yang, P.K. Liaw, Corrosion-resistant high-entropy alloys: a review, Metals-Basel 7 (2017) 43, https://doi.org/10.3390/met7020043.
[3] X.-W. Qiu, C.-G. Liu, Microstructure and properties of Al2CrFeCoCuTiNix high-entropy alloys prepared by laser cladding, J. Alloy Compd. 553 (2013) 216–220, https://doi.org/10.1016/j.jallcom.2012.11.100.
[4] M.-H. Chuang, M.-H. Tsai, W.-R. Wang, S.-J. Lin, J.-W. Yeh, Microstructure and wear behavior of AlxCo1.5CrFeNi1.5Tiy high-entropy alloys, Acta Mater. 59 (16) (2011) 6308–6317, https://doi.org/10.1016/j.actamat.2011.06.041.
[5] R. Sriharitha, B.S. Murty, R.S. Kottada, Alloying, thermal stability and strengthening in spark plasma sintered AlxCoCrCuFeNi high entropy alloys, J. Alloy Compd. 583 (2014) 419–426, https://doi.org/10.1016/j.jallcom.2013.08.176.

[6] J.-W. Yeh, S.-K. Chen, S.-J. Lin, J.-Y. Gan, T.-S. Chin, T.-T. Shun, C.-H. Tsau, S.-Y. Chang, Nanostructured high-entropy alloys with multiple principal elements: novel alloy design concepts and outcomes, Adv. Eng. Mater. 6 (5) (2004) 299–303, https://doi.org/10.1002/adem.200300567.

[7] J.-W. Yeh, Overview of high-entropy alloys, in: M.C. Gao, J.-.-W. Yeh, P.K. Liaw, Y. Zhang (Eds.), High-Entropy Alloys: Fundamentals and Applications, Springer International Publishing, Cham, 2016, pp. 1–19, https://doi.org/10.1007/978-3-319-27013-5_1.

[8] J.-W. Yeh, Alloy design strategies and future trends in high-entropy alloys, Jom-Us 65 (12) (2013) 1759–1771, https://doi.org/10.1007/s11837-013-0761-6.

[9] Y. Zhang, Y.J. Zhou, J.P. Lin, G.L. Chen, P.K. Liaw, Solid-solution phase formation rules for multi-component alloys, Adv. Eng. Mater. 10 (6) (2008) 534–538, https://doi.org/10.1002/adem.200700240.

[10] Y. Qiu, Y.J. Hu, A. Taylor, M.J. Styles, R.K.W. Marceau, A.V. Ceguerra, M. A. Gibson, Z.K. Liu, H.L. Fraser, N. Birbilis, A lightweight single-phase AlTiVCr compositionally complex alloy, Acta Mater. 123 (2017) 115–124, https://doi.org/10.1016/j.actamat.2016.10.037.

[11] J.K. Jensen, B.A. Welk, R.E.A. Williams, J.M. Sosa, D.E. Huber, O.N. Senkov, G. B. Viswanathan, H.L. Fraser, Characterization of the microstructure of the compositionally complex alloy Al1Mo0.5Nb1Ta0.5Ti1Zr1, Scripta Mater. 121 (2016) 1–4, https://doi.org/10.1016/j.scriptamat.2016.04.017.

[12] C. Stephan-Scherb, W. Schulz, M. Schneider, S. Karafiludis, G. Laplanche, High-temperature oxidation in dry and humid Atmospheres of the equiatomic CrMnFeCoNi and CrCoNi High- and medium-entropy alloys, Oxid. Met. 95 (1–2) (2021) 105–133, https://doi.org/10.1007/s11085-020-10014-7.

[13] W.R. Wang, W.L. Wang, S.C. Wang, Y.C. Tsai, C.H. Lai, J.W. Yeh, Effects of Al addition on the microstructure and mechanical property of AlxCoCrFeNi high-entropy alloys, Intermetallics 26 (2012) 44–51, https://doi.org/10.1016/j.intermet.2012.03.005.

[14] C.-Y. Hsu, C.-C. Juan, T.-S. Sheu, S.-K. Chen, J.-W. Yeh, Effect of aluminum content on microstructure and mechanical properties of Al (x) CoCrFeMo0.5Ni high-entropy alloys, Jom-Us 65 (12) (2013) 1840–1847, https://doi.org/10.1007/s11837-013-0753-6.

[15] J.Y. He, W.H. Liu, H. Wang, Y. Wu, X.J. Liu, T.G. Nieh, Z.P. Lu, Effects of Al addition on structural evolution and tensile properties of the FeCoNiCrMn high-entropy alloy system, Acta Mater. 62 (2014) 105–113, https://doi.org/10.1016/j.actamat.2013.09.037.

[16] Y.Z. Shi, B. Yang, X. Xie, J. Brechtl, K.A. Dahmen, P.K. Liaw, Corrosion of AlxCoCrFeNi high-entropy alloys: Al-content and potential scan-rate dependent pitting behavior, Corros. Sci. 119 (2017) 33–45, https://doi.org/10.1016/j.corsci.2017.02.019.

[17] H. Torbati-Sarraf, M. Shabani, P.D. Jablonski, G.J. Pataky, A. Poursaee, The influence of incorporation of Mn on the pitting corrosion performance of CrFeCoNi high entropy alloy at different temperatures, Mater. Design 184 (2019) 108170, https://doi.org/10.1016/j.matdes.2019.108170.

[18] J. Yang, J. Wu, C.Y. Zhang, S.D. Zhang, B.J. Yang, W. Emori, J.Q. Wang, Effects of Mn on the electrochemical corrosion and passivation behavior of CoFeNiMnCr high-entropy alloy system in H2SO4 solution, J. Alloy Compd. 819 (2020) 152943, https://doi.org/10.1016/j.jallcom.2019.152943.

[19] Y.-J. Hsu, W.-C. Chiang, J.-K. Wu, Corrosion behavior of FeCoNiCrCux high-entropy alloys in 3.5% sodium chloride solution, Mater. Chem. Phys. 92 (1) (2005) 112–117, https://doi.org/10.1016/j.matchemphys.2005.01.001.

[20] B. Ren, Z.X. Liu, D.M. Li, L. Shi, B. Cai, M.X. Wang, Corrosion behavior of CuCrFeNiMn high entropy alloy system in 1M sulfuric acid solution, Mater. Corros. 63 (2012) 828–834, https://doi.org/10.1002/maco.201106072.

[21] H. Luo, Z.M. Li, A.M. Mingers, D. Raabe, Corrosion behavior of an equiatomic CoCrFeMnNi high-entropy alloy compared with 304 stainless steel in sulfuric acid solution, Corros. Sci. 134 (2018) 131–139, https://doi.org/10.1016/j.corsci.2018.02.031.

[22] L. Wang, D. Mercier, S. Zanna, A. Seyeux, M. Laurent-Brocq, L. Perrière, I. Guillot, P. Marcus, Study of the surface oxides and corrosion behaviour of an equiatomic CoCrFeMnNi high entropy alloy by XPS and ToF-SIMS, Corros. Sci. 167 (2020) 108507, https://doi.org/10.1016/j.corsci.2020.108507.

[23] J. Wang, W. Li, H. Yang, H. Huang, S. Ji, J. Ruan, Z. Liu, Corrosion behavior of CoCrNi medium-entropy alloy compared with 304 stainless steel in H2SO4 and NaOH solutions, Corros. Sci. 177 (2020) 108973, https://doi.org/10.1016/j.corsci.2020.108973.

[24] E. Bettini, C. Leygraf, J.S. Pan, Nature of current increase for a CoCrMo Alloy: "transpassive" dissolution vs. water oxidation, Int. J. Electrochem. Sc. 8 (2013) 11791–11804.

[25] G. Laplanche, S. Berglund, C. Reinhart, A. Kostka, F. Fox, E.P. George, Phase stability and kinetics of σ-phase precipitation in CrMnFeCoNi high-entropy alloys, Acta Mater. 161 (2018) 338–351, https://doi.org/10.1016/j.actamat.2018.09.040.

[26] G. Laplanche, A. Kostka, C. Reinhart, J. Hunfeld, G. Eggeler, E.P. George, Reasons for the superior mechanical properties of medium-entropy CrCoNi compared to high-entropy CrMnFeCoNi, Acta Mater. 128 (2017) 292–303, https://doi.org/10.1016/j.actamat.2017.02.036.

[27] N. Wurzler, O. Sobol, K. Altmann, J. Radnik, O. Ozcan, Preconditioning of AISI 304 stainless steel surfaces in the presence of flavins—Part I: Effect on surface chemistry and corrosion behavior, Mater. Corros. 72 (6) (2021) 974–982, https://doi.org/10.1002/maco.202012191.

[28] E. McCafferty, Validation of corrosion rates measured by the Tafel extrapolation method, Corros. Sci. 47 (12) (2005) 3202–3215, https://doi.org/10.1016/j.corsci.2005.05.046.

[29] M. Langberg, C. Ornek, J. Evertsson, G.S. Harlow, W. Linpe, L. Rullik, F. Carla, R. Felici, E. Bettini, U. Kivisakk, E. Lundgren, J.S. Pan, Redefining passivity breakdown of super duplex stainless steel by electrochemical operando synchrotron near surface X-ray analyses, Npj Mat. Degrad. 3 (2019) 22, https://doi.org/10.1038/s41529-019-0084-3.

[30] A. Fattah-Alhosseini, N. Attarzadeh, the mechanism of transpassive dissolution of AISI 321 stainless steel in sulphuric acid solution, Int. J. Electrochem. 2011 (2011) 1–9, https://doi.org/10.4061/2011/521384.

[31] David R. Lide, CRC Handbook of Chemistry and Physics, Internet Version, CRC Press, Boca Raton, FL, 2005.

[32] S. Esmailzadeh, M. Aliofkhazraei, H. Sarlak, Interpretation of cyclic potentiodynamic polarization test results for study of corrosion behavior of metals: a review, Prot. Met. Phys. Chem.+ 54 (5) (2018) 976–989.

[33] X. Li, P. Zhou, H. Feng, Z. Jiang, H. Li, K. Ogle, Spontaneous passivation of the CoCrFeMnNi high entropy alloy in sulfuric acid solution: the effects of alloyed nitrogen and dissolved oxygen, Corros. Sci. 196 (2022) 110016, https://doi.org/10.1016/j.corsci.2021.110016.

[34] Y.Z. Shi, L. Collins, R. Feng, C. Zhang, N. Balke, P.K. Liaw, B. Yang, Homogenization of AlxCoCrFeNi high-entropy alloys with improved corrosion resistance, Corros. Sci. 133 (2018) 120–131, https://doi.org/10.1016/j.corsci.2018.01.030.

[35] V. Hasannaeimi, S. Mukherjee, Galvanic corrosion in a eutectic high entropy alloy, J. Electroanal. Chem 848 (2019) 113331, https://doi.org/10.1016/j.jelechem.2019.113331.

[36] V.F. Lvovich, Electrochemical Impedance Spectroscopy (EIS) applications to sensors and diagnostics, in: G. Kreysa, K.-I. Ota, R.F. Savinell (Eds.), Encyclopedia of Applied Electrochemistry, Springer, New York, NY, 2014, pp. 485–507, https://doi.org/10.1007/978-1-4419-6996-5_67.

[37] S. Joiret, M. Keddam, X.R. Nóvoa, M.C. Pérez, C. Rangel, H. Takenouti, Use of EIS, ring-disk electrode, EQCM and Raman spectroscopy to study the film of oxides formed on iron in 1 M NaOH, Cem. Concr. Compos. 24 (1) (2002) 7–15.

[38] Y.-M. Chen, N.G. Rudawski, E. Lambers, M.E. Orazem, Application of impedance spectroscopy and surface analysis to obtain oxide film thickness, J. Electrochem. Soc. 164 (9) (2017) C563–C573, https://doi.org/10.1149/2.1061709jes.

[39] W.R. Wang, J.Q. Wang, Z.H. Sun, J.T. Li, L.F. Li, X. Song, X.D. Wen, L. Xie, X. Yang, Effect of Mo and aging temperature on corrosion behavior of (CoCrFeNi)(100–x) Mo-x high-entropy alloys, J. Alloy Compd. 812 (2020), https://doi.org/10.1016/j.jallcom.2019.152139.

[40] Y.u. Fu, C. Dai, H. Luo, D. Li, C. Du, X. Li, The corrosion behavior and film properties of Al-containing high-entropy alloys in acidic solutions, Appl. Surf. Sci. 560 (2021) 149854, https://doi.org/10.1016/j.apsusc.2021.149854.

[41] M. Ray, V.B. Singh, Effect of sulfuric acid on corrosion and passivation of 316 ss in organic solution, J. Electrochem. Soc. 158 (11) (2011) C359, https://doi.org/10.1149/2.047111jes.

[42] C.A. Della Rovere, J.H. Alano, R. Silva, P.A.P. Nascente, J. Otubo, S.E. Kuri, Characterization of passive films on shape memory stainless steels, Corros. Sci. 57 (2012) 154–161, https://doi.org/10.1016/j.corsci.2011.12.022.

[43] B. Hirschorn, M.E. Orazem, B. Tribollet, V. Vivier, I. Frateur, M. Musiani, Constant-phase-element behavior caused by resistivity distributions in films II. Applications, J. Electrochem. Soc. 157 (2010) C458–C463, https://doi.org/10.1149/1.3499565.

[44] S.A. Makhlouf, Z.H. Bakr, H. Al-Attar, M.S. Moustafa, Structural, morphological and electrical properties of Cr2O3 nanoparticles, Mater. Sci. Eng. B-Adv. 178 (6) (2013) 337–343, https://doi.org/10.1016/j.mseb.2013.01.012.

[45] M.M. Abdullah, F.M. Rajab, S.M. Al-Abbas, Structural and optical characterization of Cr2O3 nanostructures: evaluation of its dielectric properties, Aip. Adv. 4 (2) (2014) 027121, https://doi.org/10.1063/1.4867012.

[46] Z. Han, W. Ren, J. Yang, A. Tian, Y. Du, G. Liu, R. Wei, G. Zhang, Y. Chen, The corrosion behavior of ultra-fine grained CoNiFeCrMn high-entropy alloys, J. Alloy Compd. 816 (2020) 152583, https://doi.org/10.1016/j.jallcom.2019.152583.

[47] V. Maurice, H. Peng, L.H. Klein, A. Seyeux, S. Zanna, P. Marcus, Effects of molybdenum on the composition and nanoscale morphology of passivated austenitic stainless steel surfaces, Faraday Discuss. 180 (2015) 151–170, https://doi.org/10.1039/C4FD00231H.

[48] E. Gardin, S. Zanna, A. Seyeux, A. Allion-Maurer, P. Marcus, Comparative study of the surface oxide films on lean duplex and corresponding single phase stainless steels by XPS and ToF-SIMS, Corros. Sci. 143 (2018) 403–413, https://doi.org/10.1016/j.corsci.2018.08.009.

[49] C.-O.-A. Olsson, D. Landolt, Passive films on stainless steels—chemistry, structure and growth, Electrochim. Acta 48 (9) (2003) 1093–1104, https://doi.org/10.1016/S0013-4686(02)00841-1.

[50] T. Yamashita, P. Hayes, Effect of curve fitting parameters on quantitative analysis of Fe0.94O and Fe2O3 using XPS, J. Electron Spectrosc. Relat. Phenom. 152 (1-2) (2006) 6–11, https://doi.org/10.1016/j.elspec.2006.02.002.

[51] P.S. Bagus, C.J. Nelin, C.R. Brundle, B.V. Crist, N. Lahiri, K.M. Rosso, Combined multiplet theory and experiment for the Fe 2p and 3p XPS of FeO and Fe2O3, J. Chem. Phys. 154 (9) (2021) 094709, https://doi.org/10.1063/5.0039765.

[52] A. Kocijan, Č. Donik, M. Jenko, Electrochemical and XPS studies of the passive film formed on stainless steels in borate buffer and chloride solutions, Corros. Sci. 49 (5) (2007) 2083–2098, https://doi.org/10.1016/j.corsci.2006.11.001.

[53] S. Tanuma, C.J. Powell, D.R. Penn, Calculations of electron inelastic mean free paths. 2. Data for 27 elements over the 50–2000-Ev range, Surf. Interface Anal. 17 (1991) 911–926, https://doi.org/10.1002/sia.740171304.

[54] C.J. Powell, A. Jablonski, NIST electron inelastic-mean-free-path database, in: N.A. O.S.A. Technology (Ed.), Gaithersburg, MD, 2010, https://doi.org/10.18434/T48C78.

[55] J.H. Scofield, Hartree-Slater subshell photoionization cross-sections at 1254 and 1487 eV, J. Electron Spectrosc. Relat. Phenom. 8 (2) (1976) 129–137, https://doi.org/10.1016/0368-2048(76)80015-1.